Article

New Insights into the Geochemical Processes Occurring on the Surface of Stuccoes Made of Slaked Lime Putty

Luciana Pocostales [1], Àfrica Pitarch Martí [2,3,*] , Núria Guasch-Ferré [2] , María Teresa Doménech-Carbó [4] and José Luís Prada Pérez [5]

[1] Independent Researcher, 08450 Llinars del Vallès, Spain
[2] Departament d'Arts i Conservació-Restauració, Facultat de Belles Arts, Universitat de Barcelona, c/Pau Gargallo 4, 08028 Barcelona, Spain
[3] Institut d'Arqueologia de la Universitat de Barcelona, c/Montalegre 6-8, 08001 Barcelona, Spain
[4] Institut Universitari de Restauració del Patrimoni, Universitat Politècnica de València, Camino de Vera s/n, 46022 Valencia, Spain
[5] Escola Superior de Conservació i Restauració de Béns Culturals de Catalunya, c/ d'Aiguablava, 109-113, 08033 Barcelona, Spain
* Correspondence: africa.pitarch@ub.edu

Abstract: The fresco technique performed with slaked lime putty as binding material has been well known since Antiquity. However, the geochemical processes that occur on the surface have been generally described as part of the carbonation process of the intonaco itself. When approaching this technique from experimental archaeology, it has been observed for the first time that during the execution period (from 0 to 20 h, approximately) the processes occurring on the surface of the stucco are different from those occurring inside. Furthermore, these processes lead to the formation of an epigenetic film of specific texture, stiffness and compactness. This study investigates the formation and evolution of this surface film using a series of slaked lime putty stucco test tubes. Samples were extracted at different intervals and subsequently analyzed by polarized optical microscopy, scanning electron microscopy, and Fourier transform infrared spectroscopy. Results indicate that the development of the film, composed of an amorphous gel-like stratum and a micro-crystalline stratum, occurs in parallel to the carbonation occurring inside the stucco. Moreover, this process does not respond to the classical geological processes of calcium carbonate formation. It was also observed that its presence slows down the carbonation in the underlying strata (*intonaco, intonachino, arriccio*, etc.) and that the surface becomes more crystalline over time. The identification of this film has implications for the field of the conservation–restoration of fresco paintings and lime-based wall paintings.

Keywords: fresco technique; stucco; carbonation process; epigenetic film; POM; SEM; FTIR

1. Introduction

Studies conducted to date on lime carbonation [1–20] note that the aerial carbonation of slaked lime putty does not occur continuously from the surface inwards but is instead a discontinuous process that follows the well-known Liesegang carbonation pattern [7]. This mechanism for the formation of calcium carbonates is produced by the diffusion of reagents via a colloidal phase that fills the pores and interparticle spaces in the mortar. Consequently, calcite crystals are precipitated in the form of rings at regular time intervals. These rings have been detected in slaked lime putties [7,17], but this phenomenon does not explain the mineral ontogenesis of the aqueous film that appears on the surface of the mortar.

Amongst the investigations that have looked into the mechanisms related to the aerial carbonation of lime, those focused on the reaction rate and mineral phase modifications of lime carbonation in real time are remarkable. Cizer et al. [21] proposed the use of thin layers

of $Ca(OH)_2$ water solution on glass slides for studying the behavior of $Ca(OH)_{2(ac)}$-$CO_{2(atm)}$ system in the short time. According to these authors, in this process, the transformation of portlandite ($Ca(OH)_2$) into calcite ($CaCO_3$) occurs in three phases: initially, there is a high uptake of CO_2 on the surface that generates calcite precipitation but which quickly becomes passive due to the formation of amorphous $CaCO_3$ (ACC) on the faces of the portlandite crystals. After that, a decrease in the rate of CO_2 uptake is observed together with a consequent reduction in $CaCO_3$ formation. Finally, CO_2 diffusion occurs through the created stratum, giving rise to a new, slower carbonation phase. These studies also show that the carbonation rate of slaked lime is faster than that of powdered lime and that this is related to the morphology of portlandite crystal. This is due to the growth of portlandite crystals soaked in water favoring the development of well-shaped crystals, especially in terms of faces 100, 101 and 001, which are the most reactive due to higher atomic density (Bravais law) [16,22]. After this seminal work, new experiments have been reported using a similar method, i.e., based on the study of the $Ca(OH)_{2(ac)}$-$CO_{2(atm)}$ system behavior in $Ca(OH)_2$ water solution droplets deposited on glass slides [23,24]. However, the results obtained [21,23,24] refer to a thin layer or droplet of slaked lime putty spread on a microscope slide. The goal of this study is to characterize the mechanisms for which the aqueous surface film is formed in real conditions on a stucco. We also describe the subsequent stages that take place in the $Ca(OH)_{2(ac)}$-$CO_{2(atm)}$ system during the execution of a true stucco prepared with traditional raw materials. It is worth emphasizing the novelty of the analytical procedure for monitoring the behavior of the $Ca(OH)_{2(ac)}$-$CO_{2(atm)}$ system in the first 24 h, which has been the subject of a patent [25]. This methodology has been extended to establish how the $Ca(OH)_{2(ac)}$-$CO_{2(atm}$ system evolves in the long term.

2. Materials and Methods

To study the formation and development of this aqueous surface film, slaked lime stucco test tubes were prepared from which samples were extracted at different intervals. These samples were subsequently analyzed as described below.

2.1. Test Tubes

The slaked lime stucco specimens were produced using traditional materials and techniques. Table 1 presents the materials used, as well as a description. These were produced by following the fresco technique procedure, which requires prior preparation of a series of layers of slaked lime and salt-free sand or marble dust on which the final touch is performed (brushing with water). The mixture used for the innermost layers contains larger sand aggregates and in greater proportions than the subsequent layers. This proportion is progressively decreased until reaching the surface, where aggregate is no longer incorporated. Figure 1a presents a cross-section of the test tube, showing the succession of layers, namely, *arriccio*, intermedium, *intonaco*, *intonachino* and epigenetic superficial film. The proportions of slaked lime to sand in each and the aqueous film that is produced on the surface are also included.

Table 1. Technical features of materials used to make the test tubes.

Material	Description
Binding material	Lime putty paste CL 90 PL. supplier: Cales Segarra y Hernández, Barcelona. UNE-EN 459-1. Calcium hydroxide (portlandite) embedded in an aqueous colloidal dispersion composed of carbonate and hydroxyl ions.
Aggregate	Siliceous sand *. Granulometry: 4–2.5 mm and 250 μm.
Solvent	Bezoya®® weakly mineralised natural mineral water. Chemical composition (in mg/L): dry residue at 180 °C: 28; bicarbonates: 7; chlorides: 0.87; Ca: 2.73; Mg: 0.39; Na: 2.55; Si: 11.0.
Supporting material	Unglazed brick. The supporting material was grooved on the back to help the stucco to adhere. Dimensions: 27.5 × 13.5 × 1 cm.

* A siliceous material was used to avoid having to discriminate the calcite from the aggregate.
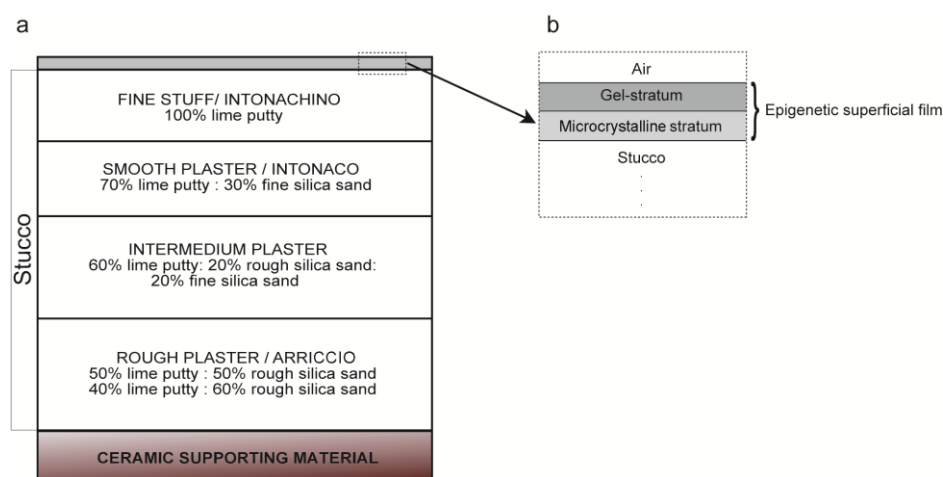
Figure 1. (**a**) Stratigraphy of a typical stucco test tube. The square denotes the area enlarged in (**b**) that delimits the thin film studied in the present investigation formed on the surface of the *intonachino* (upper stucco layer).

2.2. Conditions for Execution of Test Tubes and for Extraction and Conservation of Samples

2.2.1. Environmental Conditions

In order to generate inter-comparable data and to be able to assess how the aqueous surface film evolves in real time, specific conditions were established in terms of temperature (21 °C) and relative humidity (60–65%). These conditions were maintained from the moment of execution of the test tubes until the extraction of the samples.

2.2.2. Time Sequence

To determine the evolution of the stucco surface, the time period that needs to be studied had to be established first. This involved a preliminary study of a test tube for which organoleptic observation enabled us to define five evolutionary phases on the surface (Table 2). During the first three phases (between 0 and 24 h), a more rapid evolution of the stucco surface was observed. Hence, the interval of sample extraction between 0 and 24 h was performed following the logarithm of 24 [7,26,27]. From the fourth phase (>24 h) onwards, sample extraction was performed every 24 h for 7 days, gradually reducing the number of samples as shown in Table 3.

Table 2. Evolution over time of the surface of a slaked lime putty stucco.

Phase	Interval	Macroscopic Observations
1	0–60 m	Film development starting from the initial raw material prior to construction through 60 min after construction.
2	1–4 h	Beginning of film hardening and decrease in plasticity.
3	4–24 h	Formation and development of the film. At the end of this process, the surface, which was partially permeable, did not allow the pigment particles to adhere.
4	1–30 d	Hardening of the film.
5	>90 d	Long-term film development.

m—minutes; h—hours; d—days.

For the POM study, samples were extracted from the same test tube. For the FTIR and SEM, the "young" samples were removed from test tubes specially prepared for the occasion, while the "aged" ones were extracted from the same test tube used for POM. All test tubes were made following the same procedure and by using the same slaked lime and aggregate, so that they featured the same characteristics.

Table 3. Extracted samples from the test tubes.

Sequence	Interval of Extraction	Number of Extracted Samples
0–1 h	3 m 20 s	19
1–2 h	10 m	6
2–3 h	30 m	2
4–24 h	60 m	20
24 h–7 d	24 h	6
8–30 d	48 h	11
90 d		1
160 d		1
TOTAL		66

s—seconds; m—minutes; h—hours; d—days.

2.2.3. Extraction System

Samples were extracted and encapsulated in accordance with the protocol described by [25]. This procedure guarantees isolation of the samples from the CO_2 in the air, thus interrupting their evolution and permitting observation and analysis of the different physical–chemical transformation processes. Moreover, this does not deform them and enables subtraction of the surface layer under study.

2.3. Instrumentation

To optically and morphologically characterize the evolution of the components of the aqueous surface film, a polarized optical microscope (POM) PM-2085 by Motic was used, equipped with four lenses ($40\times$, $100\times$, $400\times$ and $1000\times$), including crossed (XP) and parallel (PP) polarizers, two λ and $1/4$ λ accessory plates and a Bertrand lens. It also featured an attached Moticam 1 sp 1.3 MP digital camera for on-screen observation and image capture.

Compositional and morphological characterization of smaller size particles (<0.5 μm) was performed with a scanning electron microscope (SEM) EVO ®® MA 10. Observations were performed under vacuum conditions with a voltage of 20 k.

Identification of compounds, determination of their relative concentrations and degree of disorder of the lattice of formed calcium carbonate particles were carried out using a Fourier transform infrared (FTIR) spectrometer VERTEX 70 (Bruker Optics). This instrument included a fast recovery deuterated triglycine sulphate (FRDTGS) temperature-stabilized coated detector and an MKII Golden Gate Attenuated Total Reflectance (ATR) accessory. Thirty-two scans were collected at a resolution of 4 cm^{-1}. IR spectra from three different replicates were acquired at each time to control and measure the advance of the carbonation process in the specimens prepared. Processing of the IR spectra was performed using the OPUS 7.2/IR software (Bruker Optik GmbH, Ettlingen, Germany).

To discern the IR bands of calcite and amorphous calcium carbonate embedded in the ν_3 stretching band of carbonate, we applied the curve-fitting method. The algorithm of Levenberg-Marquardt, based on the least squares method, was employed. Between the two possible Gauss and Lorentz band shapes, the former was selected, as it provided the best results.

3. Results and Discussion

3.1. POM

The POM study was used to characterize the epigenetic film that forms on the stucco surface and observe its mineral ontogenesis. It was thus determined that this film evolves from an initial aqueous dispersion and transforms into two defined strata of a few microns: a shallower stratum made up of amorphous compounds (hereinafter "gel-like stratum") and an underlying microcrystalline stratum (hereinafter "microcrystalline stratum") (Figure 1b). Figure 2 shows the different particles identified in both strata. A detailed description of each stratum is presented below:

- Gel-like stratum:
  - ○ External face (Figure 2a): It is exposed to the atmosphere. Translucent, with a microgranular texture and low birefringence, it is composed of a nebula of sub-micrometer particles that, in association with each other, present an incipient anisotropy. It is observed from 3 min after the execution of the stucco. As it evolves, it increases both in thickness and birefringence, acquiring a soft golden hue over time. Formation of this nebula does not seem to depend on standard aerial carbonation processes that require longer timeframes as stated by [21].
  - ○ Internal face (Figure 2b): It is composed of a granular mass of sub-micrometric crystals.
- Underlying microcrystalline stratum: It is located between the gel-like stratum and the stucco surface and formed by crystalline aggregates of different kinds:
  - ○ Aggregates of particles with an amoeboid, botryoidal morphology (Figure 2c–f) arising from the components of slaked lime (carbonate nanocrystals, colloidal particles and crystalline nuclei) generated during the drying process. These appear between 3 and 15 min after the execution of the stucco, by heterogeneous nucleation on the pre-existing components. Aggregates of amoeboid particles evolve via the mechanism of crystal growth in sectors [28], forming subeuhedral (botryoidal) crystals with curved faces that present black–white checkered interference colors (Figure 2g–h).
  - ○ Fibrous aggregates of acicular crystals with a polycrystalline nucleus (Figure 2i). These are observed during the first 3 min after execution. After this period, they disaggregate, giving rise to isolated crystals with an acicular, tubular morphology.
  - ○ Three-dimensional (Figure 2j) or flat (Figure 2g,k) spherulite-type fibroradial aggregates. These are observed during the first minutes after preparation of the test tube. They are of variable size but always in the micrometric order. The flat spherulites (Figure 2l) can group irregularly by stacking along the C axis. Each spherulite has a different rotation angle to the one before [28]. These crystals evolve by growth in sectors the quadrants of which can become disaggregated.

3.2. SEM

While the POM analysis provided a considerable amount of information about the epigenetic surface film, it was sometimes challenging to identify the layer on which the observations were being made. SEM study was used to accurately identify the different particles previously detected by POM and chemically characterize the set of strata that constitutes the film (Figure 3).

The gel-like stratum is made up of calcium carbonate *(vide infra)*, whose particle size is in the nanometric range and which forms the translucent nebula observed by POM (Figure 2a). Under the SEM, this nebula is initially characterized on its outer face by the presence of amoeboid particles arranged in a discontinuous manner. Between 12 and 24 h after preparing the test tube, the stratum acquires a gel-like, micro-porous appearance and is made up of flaky, interpenetrated particles. Columnar growths are also observed but only on the inner face of the gel-like stratum, following the growth patterns of floating calcite described by [29] as shown in Figures 3 and 4. This gel-like stratum stabilizes physicochemically over time (>160 d).
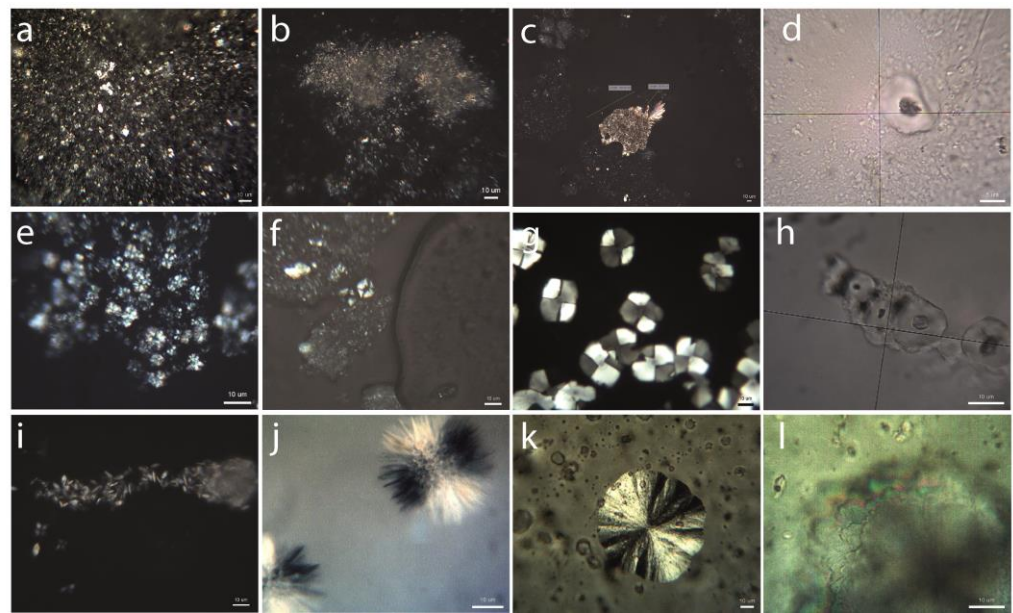
Figure 2. Crystalline specimens and other particles observed on the epigenetic surface film formed in the *intonachino* by POM. (**a**). External face of the gel-like stratum featuring a cryptocrystalline texture; (**b**). Internal face of the gel-like stratum with a microgranular texture; (**c**). Prismatic hexagonal crystal (portlandite) in process of dissolution/transformation; (**d**) Particle showing heterogeneous growth nucleus; (**e**) Botryoidal aggregates; (**f**) Amoeboid aggregates; (**g**) Sectorial-structure crystal aggregates; (**h**) Sectorial-structure chain-like aggregates; (**i**) Lenticular and rhombohedral crystal aggregates; (**j**) Acicular-radial aggregates; (**k**) Lamellar-radial spherulite; (**l**) Axial stacking of lamellar-radial spherulite.
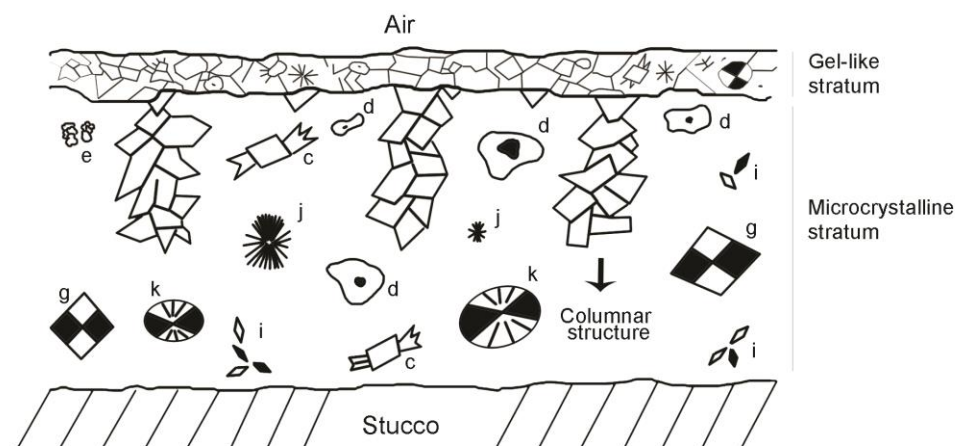

Figure 3. Sketch of the epigenetic superficial film in section. Letters correspond to the crystalline phases and other particles shown in Figure 2 (modified from [29]). Note that although the gel-like stratum is mainly composed of sub-micron particles of calcium carbonate *(vide infra)*, some of the crystallochemical phases identified in the microcrystalline stratum may be also present in the outermost layer. Letters correspond to crystalline specimens and other particles shown in Figure 2.
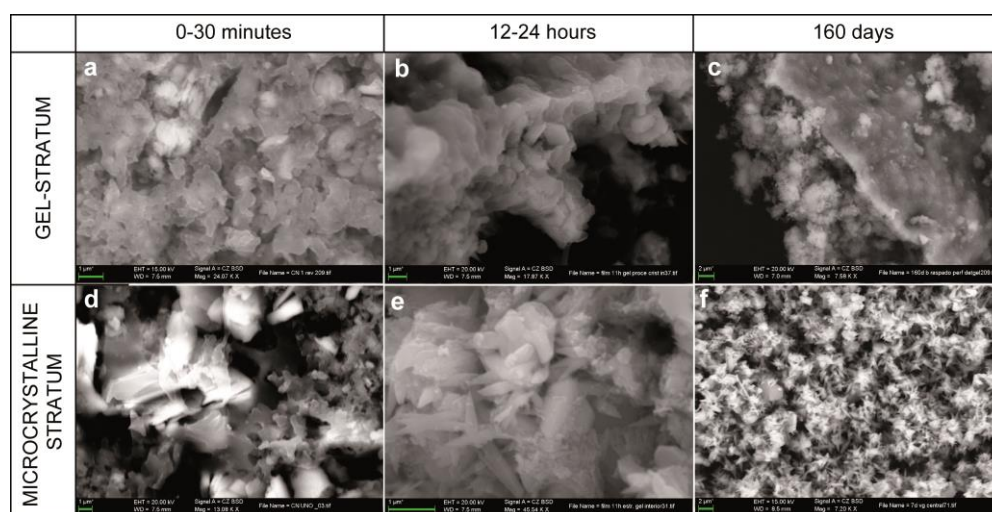
Figure 4. Evolution of texture developed in the gel-like stratum (**a**–**c**) and the microcrystalline stratum (**d**–**f**), both on the surface of a lime putty plaster. Images obtained by SEM. (**a**) Initial development of the gel-like stratum 30 min after application; (**b**) Growth of columnar structures on the inner side of the gel-like stratum 12–24 h after application; (**c**) Gel-like stratum after 160 days; (**d**) Initial development of microcrystalline interphase between the gel-like stratum and the surface of the slaked lime plaster; (**e**) Growth of various crystalline morphologies previously described by POM; (**f**) Advanced crystal development.

Regarding the underlying microcrystalline stratum, SEM study (Figure 4) has confirmed the typological variety previously established with POM and enabled better observation thereof. In addition to the crystals described in the previous section, the presence of acicular and lenticular crystals were identified inside the interstitial spaces. These largely develop on the faces of the euhedral and sub-euhedral crystals that arise from the disaggregation of sectoral crystals and which contribute to the densification of the stratum.

3.3. FTIR Spectroscopy

The analysis with this technique enabled the identification of the compounds present in the studied epigenetic surface films and the characterization of their structural changes. IR absorption spectra of the epigenetic surface film were acquired along the drying process of the test tubes. The time program was as follows: 1, 3, 6, 12, 30 min; 1, 4, 8, 16, 24 h, and 160 days (3840 h). To characterize the IR bands occurring in the IR spectra, the experimental values of the band maximum were compared to those reported in the literature [23,30–38]. Table 4 shows a summary of the specific frequency values for the diagnostic vibration modes of calcium hydroxide (portlandite), the different types of calcium carbonate reported in the literature and the values obtained in this study.

Table 4. Diagnostic IR band frequencies obtained in this study and from the literature [30–38].

Frequencies $\cup$ (cm^{-1})						Assignation	Related Compound
ACC [23,30,36,37]	Portlandite [33,34]	Calcite [32,34,35]	Aragonite [35]	Vaterite [31,35]	Monohydro- calcite [38]		
-	3646 w(sp) *3640*				3400,	Stretching vibration OH in Ca(OH)$_2$	Calcium hydroxide
-	3450 vs. (b), 3400 vs. (b) *3330*				3327 s(b)	Stretching vibration OH	Calcium hydroxide
-	1650 m(b), 1620 m(b) *1637*	-	-	-	1700 w(b)	Bending vibration OH in Ca(OH)$_2$	Calcium hydroxide

Table 4. *Cont.*

Frequencies υ (cm^{-1})						Assignation	Related Compound
ACC [23,30,36,37]	Portlandite [33,34]	Calcite [32,34,35]	Aragonite [35]	Vaterite [31,35]	Monohydro-calcite [38]		
1470, 1490 (sh), 1425 vs. (b) *1470–1490sh,1420*		1425 vs. (b) *1420*	1500 vs.	1450 vs.	1492 vs. 1401 s(b)	ν_3—asymmetric stretching vibration of carbonate group	Calcium carbonate
1084 vw(sp)			1083 vw(s)	1087 vw(s)	1063 w(s)	ν_1—symmetric stretching vibration of carbonate group	Calcium carbonate
874 m(sp) *872*		845 w(sp), 875 m(sp) *872*	844 w(sp), 874 m(sp)	876 m(sp) s	872 m(s)	ν_2—asymmetric bending vibration of carbonate group	Calcium carbonate
725 vw or absent (sp), 690 (sh) *absent*		712 w(s) *712*	700 w(sp), 712 w(sp)	744 m(sp)	762 m, 698 m(s)	ν_4—symmetric bending vibration of carbonate group	Calcium carbonate

Acronyms: ACC—amorphous calcium carbonate; Intensity: vs.—very strong; s—strong; m—medium; w—weak; vw—very weak. Morphology: sp—sharp; b—broad; (sh)—shoulder. Values obtained in this study in italics.

Figure 5 shows the sequence of IR spectra acquired along the time interval in the study. This illustrates the evolution of the composition of the epigenetic surface film. The progress in the carbonation reaction can be followed through the gradual reduction in the intensity of the hydroxyl bands in the calcium hydroxide together with the concomitant increase of the carbonate group bands in the newly formed calcium carbonate particles.
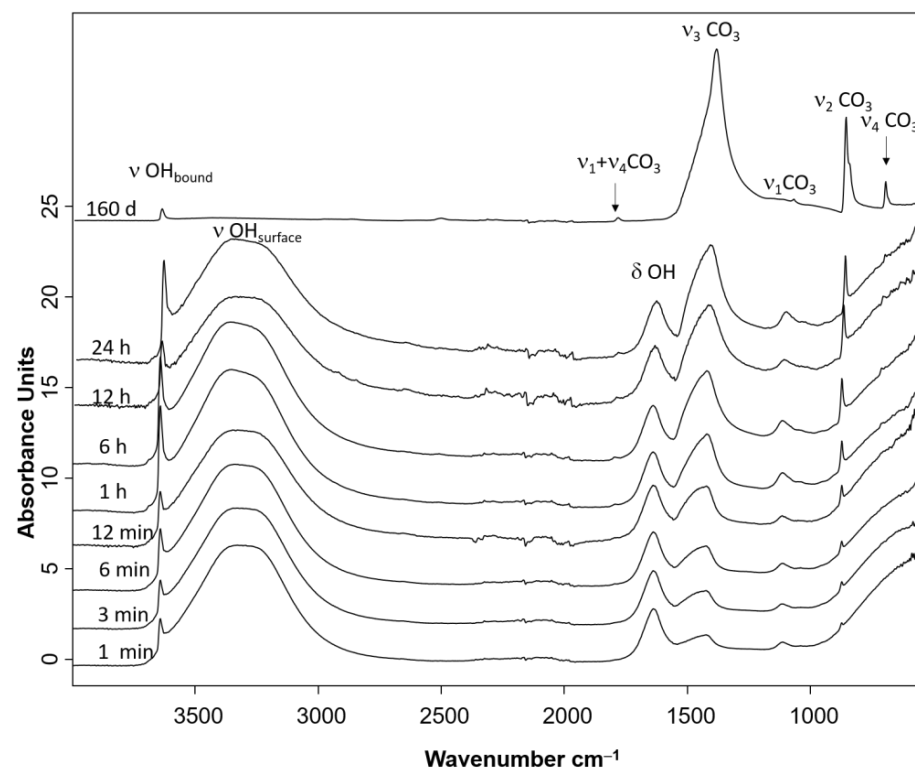

Figure 5. Sequence of IR spectra acquired within the first 24 h and after 160 days.

The main changes are observed in the IR spectra shown in Figure 6a, acquired at 1 min, 24 h, and 160 days. The IR spectrum of the sample obtained at the beginning of the experiment is dominated by the absorption bands corresponding to the stretching (3640 and 3300 cm^{-1}) and bending (1637 cm^{-1}) vibrations of the hydroxyl bound and surface hydroxyl groups associated with calcium hydroxide in suspension. IR absorption bands of the carbonate group in calcite and its polymorphs are occurring in the three shown spectra. In particular, ν_3, ν_2, and ν_4 vibration bands, the three symmetry-allowed phonon

modes of calcium carbonate, are used for diagnostic purposes. They are characterized more accurately in Figure 6b. The progressive increase over time of the broad ν_3 stretching carbonate band with the maximum at 1420 cm^{-1} can be seen, as well as the sharp ν bending band at 872 cm^{-1} and the growth of the ν_4 bending band at 712 cm^{-1}, almost absent at the beginning (Figures 5 and 6). According to data listed in Table 4, the experimental values found in these spectra correspond to calcite.
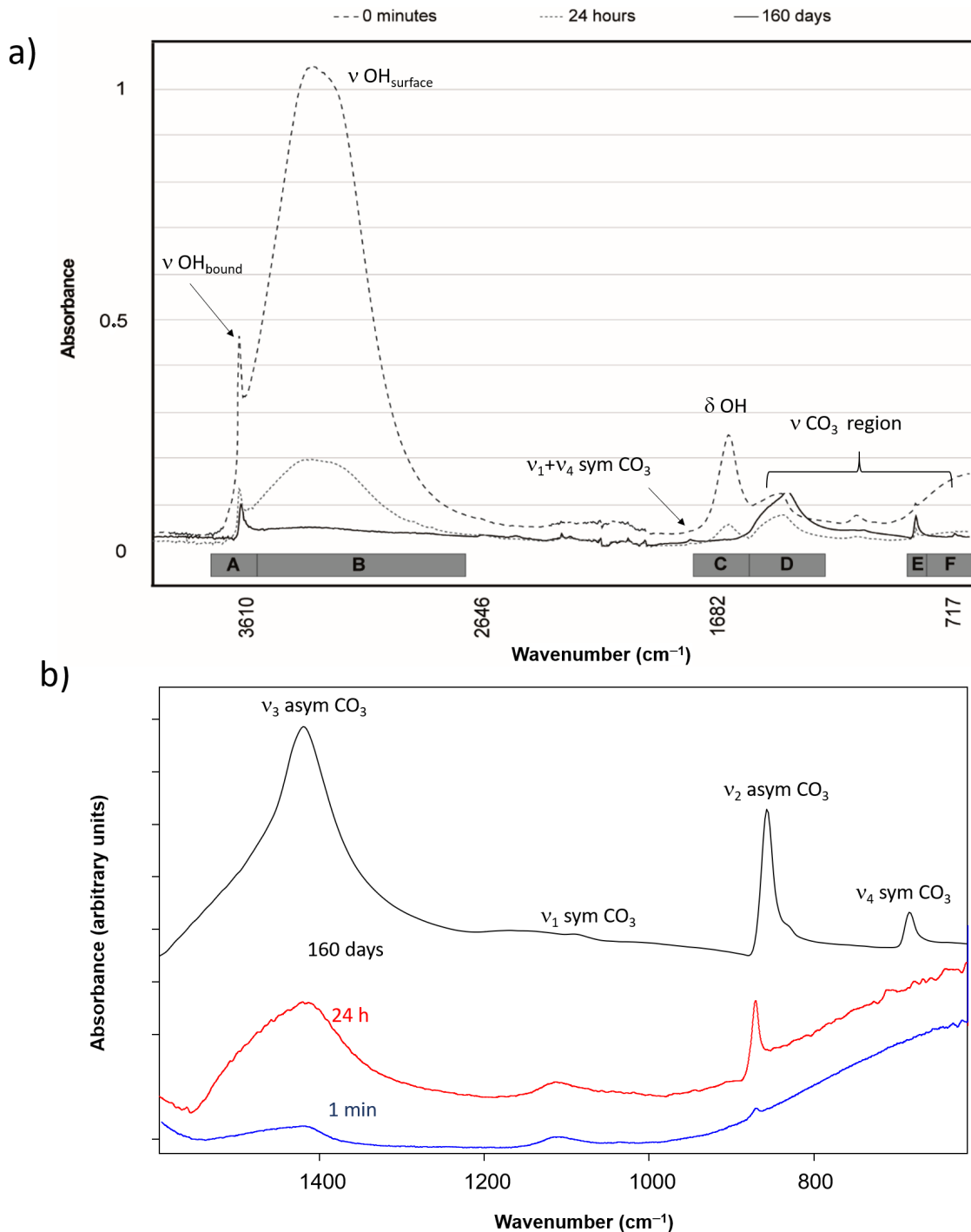
Figure 6. (**a**) IR spectra of samples taken from the surface of test tubes initially, after 24 h and after 160 days; (**b**) Detail of the 1500–600 cm^{-1} region for the IR spectra.

The asymmetry observed in the shape of the broad ν_3 stretching carbonate band suggests that it is composed of at least two overlapped bands ascribed to ACC with

maxima at 1470–1490 cm^{-1} and C + ACC with the maximum at 1420 cm^{-1}. This hypothesis has been confirmed by applying the iterative method of curve fitting on the ν_3 stretch band. Figure 7A(a–f) show the original overlapped band, the sum spectra obtained iteratively, and the two bands that compose the theoretical sum band obtained in the IR spectra acquired in the first 12 h. The individual bands exhibit maxima in the ranges 1414–1423 and 1451–1496 cm^{-1}, approaching those previously reported in the literature [36]. This confirms the presence of amorphous calcium carbonate (ACC) in the epigenetic surface film together with calcium carbonate. The excellent match of the experimental envelope band (blue line) and the theoretical sum band (red line) can be seen for all the samples with values of root mean square error in the range 0.004–0.02. It is possible to study the role of the ACC in forming the epigenetic surface film if it is assumed that there is a direct correlation between the intensity (area or height) of the overlapped bands and the assigned component. A significant difference between the ACC and C + ACC band areas is observed in Figure 7A(a,b). The greater ACC band area in the first IR spectra indicates that this compound is prevalent at this early epigenetic surface film formation stage. It is also observed that this band increases over time in the first 3 min. After this, the C + ACC band grows and surpasses the ACC band. This second step lasts 12 min (Figure 7A(c,d). The increase of the C + ACC band goes on over time until 12 h (Figure 7A(e,f)). A schematic view of the evolution of the epigenetic surface film may be observed in Figure 7B.
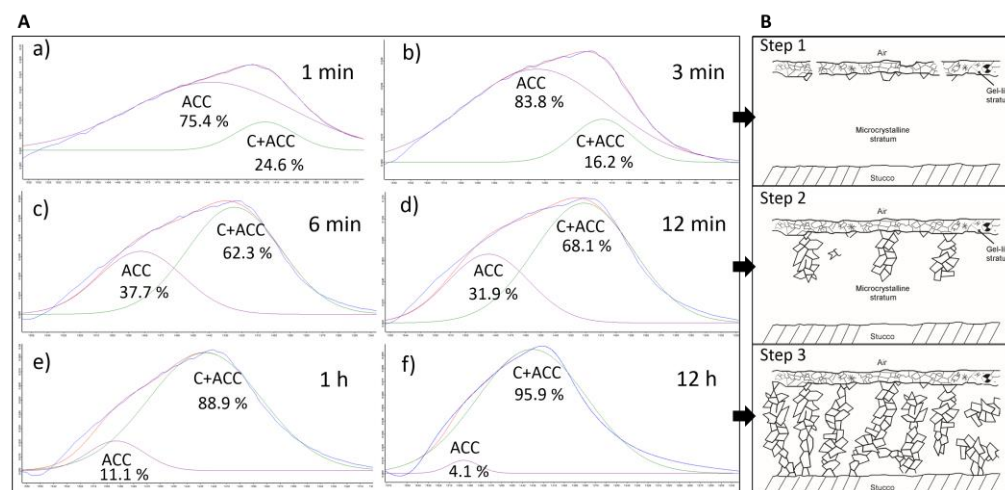

Figure 7. (**A**) Original overlapped band (blue line), sum band (red line) and individual bands of calcite plus ACC (C + ACC) (green line) and ACC (purple line) obtained by applying the mathematical curve-fitting process in the carbonate ν_3 stretching band at: (a) 1 min; (b) 3 min; (c) 6 min; (d) 1 h; (e) 1 h and (f) 12 h. Percentage values of the overlapped band area are provided. (**B**) Epigenetic superficial film at step 1 (0–3 min), step 2 (3–12 min) and step 3 (12 < time < 160 days).

Information about the behavior of the epigenetic surface film in these initial stages can also be obtained by depicting the dependence of the ACC/(C + ACC) band-area ratio versus time. Figure 8 shows that the process of epigenetic surface film formation takes place in three steps:

Step 1: There is a rapid increase of the ACC/(C + ACC) band area ratio corresponding to the initial step in which the ACC nanoparticles are generated in the epigenetic surface film from the dense supersaturated solution close to the air phase. This process is fast, spending at ca. 3 min (see insert in Figure 8). At the same time that the ACC particles are generated in the film's core, ACC nanoparticles, in contact with the air phase and, therefore, with a high supply of CO_2, form a thin upper gel-like stratum. This upper sublayer quickly becomes denser and starts to act as a barrier to the diffusion of CO_2 from the atmosphere (see Figure 7B-step1).
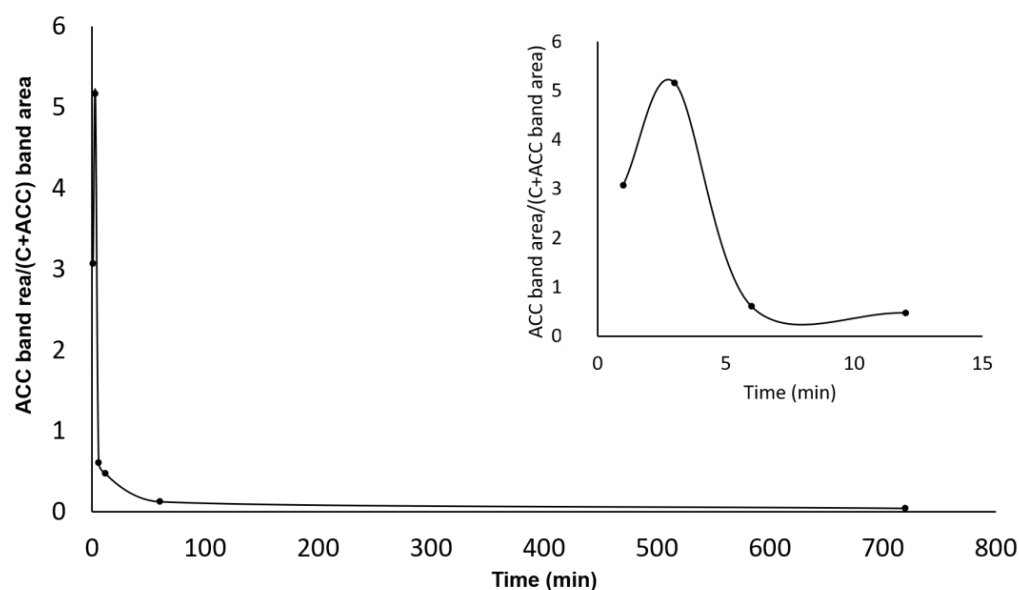
Figure 8. Percentage of individual bands of calcite versus time. Insert shows in detail the behavior in the first 12 min.

Step 2: The trend is inverted, and a decrease in the ACC/(C + ACC) band area ratio is observed (Figure 8). This second step lasts up to 12 min. This behavior is associated with the beginning of the formation of calcite grains from the precursor ACC nanoparticles and the growth of calcite particle aggregates in the underlying microcrystalline stratum (see Figure 7B-step2).

Step 3: the crystalline calcite formation rate is drastically slowed down up to 12 min. This behavior lasts up to 160 days (see Figure 7B-step3).

The evolution of the carbonation process can also be observed in the graph shown in Figure 9. It depicts the dependence of the band height (I) ratio (I_D/I_A) of the A band (I_A) to the D band (I_D) versus time. The A band is ascribed to the hydroxyl groups, and the D band (I_D) corresponds to the carbonate group (see Table 5). There is a significant formation of calcium carbonate particles within the first hour (steps 1 and 2), followed by a reduction of the velocity of the carbonation reaction until 160 days (step 3).

Table 5. Values of the IR band intensity ratio for samples obtained at different times. Values of the I_E and I_F heights were normalized to the corresponding ν_3 band value.

Time (hours)	0.48	1	4	8	16	24	3840	6480	8760
I_D/I_A	0.46	0.68	0.86	1.1	1.15	1.84	4.35		
I_E/I_F	10.8	10.78	10.4	10	8.5	7.33	5.1	4.04 *	4.03 *

(*): results obtained from [17].

A theoretical model proposed by some authors [39–42] enables a comparison of the atomic disorder degree in the calcite lattice originated by geogenic, biogenic, and anthropogenic processes. This model is based on the distinct sensitivity of the ν_2 (E) and ν_4 (F) carbonate bending bands. The ν_4 (F) carbonate bending band is more sensitive to the atomic ordering of the calcium carbonate particles. Therefore, the value of the ratio (I_E/I_F) at the maxima of ν_2 to ν_4 bending bands is a suitable indicator of the structural changes in the particles during the maturation of the epigenetic film on the stucco surface. The time interval of the curve depicted in Figure 10 has been enlarged to 365 days, including values provided by [17]. The graph shows that the I_E/I_F ratio decreases over time. This behavior indicates that the crystalline order of the particles in the epigenetic superficial film increases over time. These changes are associated with the progressive transformation of the ACC nanoparticles into calcite crystals.
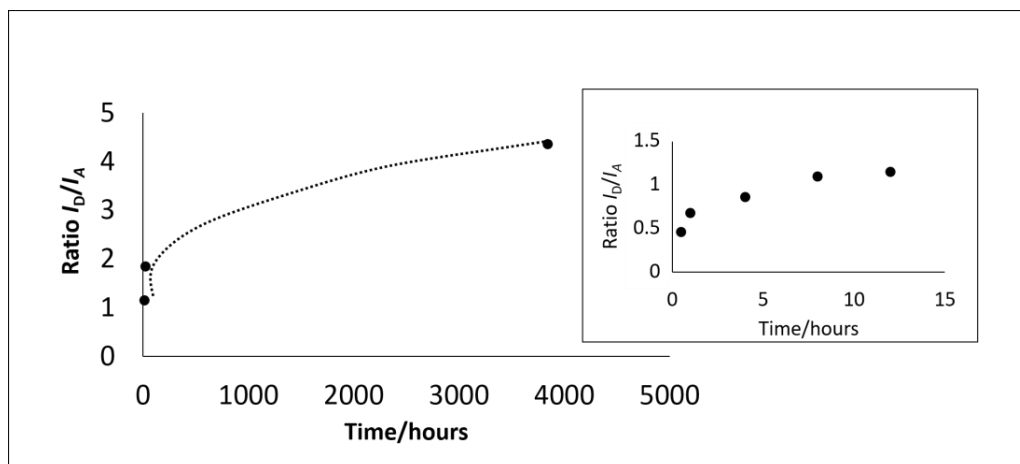
Figure 9. Diagram of the ratio of intensities of IR bands of calcium carbonate and calcium hydroxide (I_D/I_A) versus time. Insert shows in detail the 0–16 h interval.
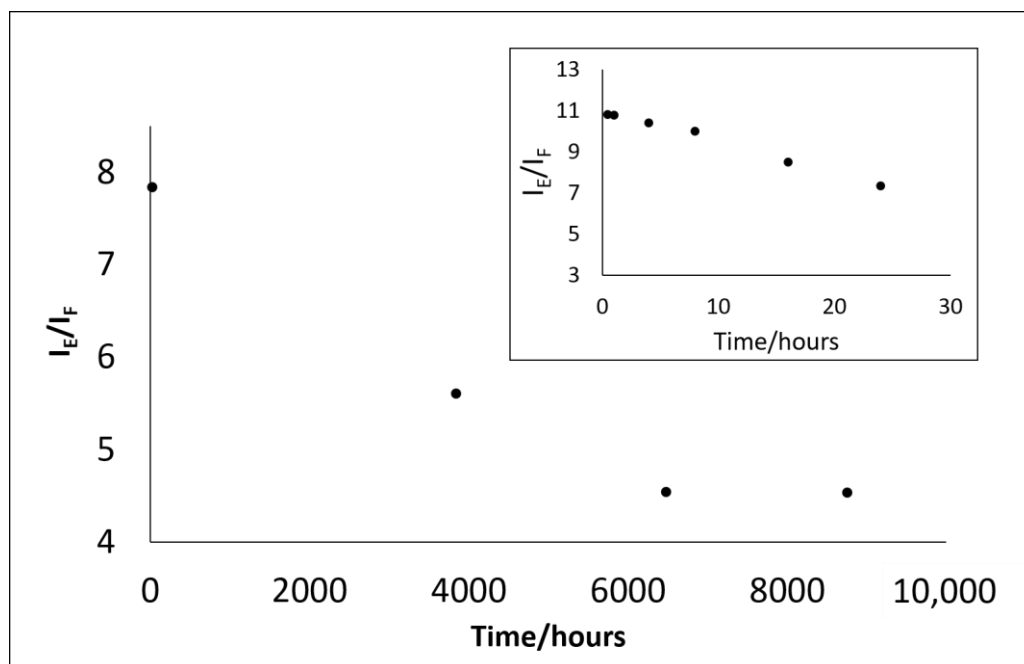

Figure 10. Diagram of the ratio of intensities of IR bands ν_2 and ν_4 of the carbonate group (I_E/I_F) versus time. Insert shows in detail the 0–24 h interval.

4. Discussion

Formation of solid calcium carbonate during stucco preparation is based on complex chemical equilibria reactions and diffusion processes that are difficult to separate and investigate independently. Two well-known theories have been proposed to describe the mechanisms by which solid calcium carbonate is formed from a supersaturated solution in different biological, geological, or industrial environments. Figure 11 shows a schematic view of the different steps proposed by both classical and non-classical theories.

The classical theory establishes that precritical clusters formed by the reversible addition of ions from the solution are nucleated, becoming a post-critical nucleus. This is only possible if specific energy and structural conditions that guarantee its stability are met [43]. The nucleation is a first-order phase transition, and nuclei form as result of the stochastic density fluctuations of a homogeneous supersaturated aqueous solution [44]. After this, nuclei become crystals through a growth process.

On the other hand, the starting point for the non-classical theory is the formation of stable precritical clusters composed of ions and other related species present in the solution to produce a postcritical nucleus. The pre-nucleation clusters are nanometer-sized. Although thermodynamically stable, the high solubility of those species results in a weak phase boundary with the surrounding solution [45]. Those nuclei undergo an internal reconfiguration, resulting in more ordered structures that can become crystalline. Further growth of these protocrystals results in the final crystal [45]. The ACC particles play an essential role the development of the polyamorph pathways used during the shell formation or the stiffening of the exoskeletal cuticle [44].
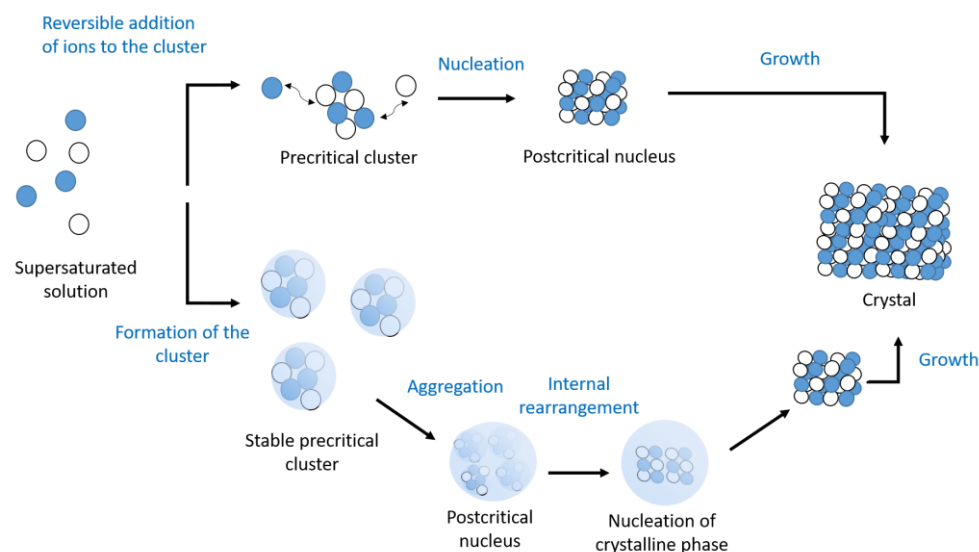
Figure 11. Schematic view of the different steps proposed by both classical and non-classical theories. Adapted from [45].

In this context, the present study investigates and establishes how the characteristic surface film forms in carbonating traditional slaked lime mortars, with a twofold goal: first, to determine the structure of this epigenetic surface film (i.e., pre-nucleation versus post-nucleation phenomena); second, to explore different instrumental methodologies for investigating the formation and evolution of this epigenetic surface film and understanding why it exhibits different characteristics from the internal stucco core.

Sequential examination at different times by POM and SEM during the drying process of the stucco was carried out on samples of the epigenetic surface film. This methodology enabled the identification of a colloidal-like suspension, composed of spherulitic nanometric particles, in the gel-like stratum within the first minutes (see Figures 2a and 4a). These particles, which should be formed by aggregation from precursor nanoparticles, have been associated with a post-critical nucleus according to the non-classical theory. These species have been previously recognized as aggregates of ACC nanoparticles in $Ca(OH)_2$ water solution drops on glass slides by SEM and FTIR [23]. The same features are also recognized in the present study in the ACC typical band in the carbonate ν_3 stretch region. Interestingly, it is observed that a blueshift of this individual band takes place over time. Figure 12 shows the evolution of the ACC band maximum over 160 days.
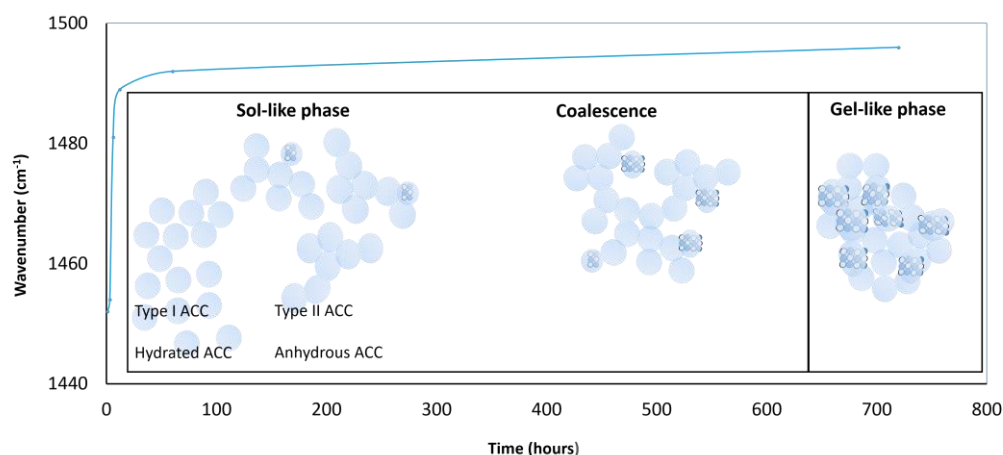
Figure 12. Maximum of the ACC band in the carbonate ν stretch region versus time. Scheme of the presumed behavior of the ACC particles when forming the gel-like stratum in the epigenetic surface film.

The first step is characterized by the rapid shift of the maximum towards higher wavelengths within the initial 60 min. Then, this value slightly increases. These changes have been tentatively correlated with the evolution of the ACC particles during the formation of the gel-like stratum composing the outer part of the epigenetic surface film. During the so-called "sol-like phase," higher CO_2 content in the slaked lime suspension/atmosphere interface promotes the development of pre-nucleation clusters and their rapid transformation to type-ACC particles. These particles with spherulitic shapes were already identified (see Figure 2a) and are characterized by the lowest band maximum wavenumber. They have been associated with type I or hydrated ACC particles. These particles are initially isolated in the solution due to the solvation with water molecules, abundant at this moment, but progressively become closer due to the rapid emergence of new ACC particles. The increase of ACC particles results in the formation of clusters of type II anhydrous ACC particles, structurally reducing their water content. In this early stage, the ACC particles remain in solution configuring a "sol-like phase." After 12 h, these micellar-sized particles evolve and behave like coalescent micelles, forming the "gel-like phase" and adopting a laminar morphology (Figure 4b,c) of vitreous appearance under POM. At this point the upper gel-like stratum is formed.

In parallel, the IR spectra showed a relative decrease in ACC content and a concomitant increase in calcite content. According to the non-classical model, this is evidence of the occurrence of internal rearrangements in the ACC aggregates. These rearrangements give rise to nucleation of the crystalline phases and further growth of the crystalline particles. This increase of crystallinity over time is confirmed by the progressive increase of the intensity of the enveloped band at 1420 cm^{-1} and the decrease of the $I\nu_2/I\nu_4$ ratio observed over time (see Figure 10). The different profiles that feature the curves displayed in Figures 8, 10 and 12 suggest that the transition of ACC into calcite crystals and the formation of the film take place through different mechanisms; therefore, their dependence over time is different. Results also suggest that the carbonation and formation of calcite crystalline particles are progressively extended through the whole epigenetic surface film, where ACC particles are also identified (see Figures 2e–l and 4d–f).

5. Conclusions

Results obtained in the present investigation indicate that the surface of a slaked lime stucco evolves in three stages in which the presence of two newly formed strata can clearly be differentiated on the surface: the surface gel-like stratum and the underlying microcrystalline stratum.

Diffusion towards the surface of the components that form the colloidal dispersion contained in the slaked lime (CO_3^{2-}, $Ca(OH)_2$ and $Mg(OH)_2$) occurs in stage 1, due to the presence of the aqueous surface film applied at the end of stucco production. This colloidal dispersion quickly becomes supersaturated due to evaporation of water. After 3 min, the epigenetic surface film begins to develop, formed on the surface by calcium carbonates of low crystalline order that could be considered amorphous (gel-like stratum), and on the inside by a liquid inter-phase that is in contact with the surface of the stucco. At the same time, the first phases of carbonation occur inside the stucco.

Stage 2 is influenced by the presence of this gel-like stratum, which acts like a semi-permeable membrane. Two faces can be distinguished in the gel-like stratum: one in contact with the air, with a gel-like texture and formed by particles of amorphous calcium carbonate, and the inner one, where hanging calcite structures develop. This last stratum conditions the carbonation process that occurs inside the stucco and favors the gradual supersaturation of the liquid inter-phase, thus giving rise to a stratum with a microcrystalline texture in which different crystalline "split growths" have been observed, such as heterogeneous nucleation processes and sectoral growths. During this stage, the mechanical properties of the surface vary, with an increase in its hardness and a decrease in its plasticity being noted. All these phenomena occur during the first 20 h. This is the moment when burnishing and/or fresco painting techniques are performed.

Finally, stage 3 is characterized by the densification of both strata (gel-like stratum and microcrystalline stratum) and the slowing down of the physicochemical processes that occur inside (mainly carbonation) as pore size is reduced. The evolution of the underlying strata that make up the stucco (*intonaco*, *intonachino*, *arriccio*, etc.) is influenced by the presence of this epigenetic surface film that slows down the standard carbonation reaction.

From a chemical point of view, results obtained by FTIR confirm the formation of an epigenetic surface film with different compositions on the stucco layer. These results agree with the rest of the analytical techniques applied in the study. The position and changes in the intensity of the bands in the IR spectra indicate that the epigenetic surface film is mainly composed of ACC particles that progressively transform into calcite crystals. The maturation process of the epigenetic film on the stucco during the drying process of the *intonachino* is described by three different and complementary approaches: the study of the profile of the I_A/I_D and I_E/I_F ratios over time, the curve-fitting method applied to the enveloped ν_3 stretch band intensity ratios, and further study of its dependence over time. These changes may be due to the evolution of the gel-like stratum itself or to the evolution of the inter-phase between the gel-like stratum and the stucco surface, which changes from a liquid phase to a solid microcrystalline stratum one.

Data Availability Statement: Not applicable.

References

1. Van Balen, K.; Van Gemert, D. Modelling lime mortar carbonation. *Mater. Struct.* **1994**, *27*, 393–398.
2. Rodriguez-Navarro, E.; Hansen, E.F.; Ginell, W.S. Calciuem hydroxide crystal evolution upon aging of lime putty. *J. Am. Ceram. Soc.* **1998**, *81*, 3032–3034. [CrossRef]
3. Cazalla, O.; Rodriguez-Navarro, C.; Sebastian, E.; Cultrone, G.; De la Torre, M.J. Aging of Lime Putty: Effects on Traditional Lime Mortar Carbonation. *J. Am. Ceram. Soc.* **2000**, *83*, 1070–1076.
4. Hansen, E.F.; Tagle, A.; Erder, E.; Baron, S.; Connell, S.; Rodriguez-Navarro, C.; Van Balen, K. Effects of aging on lime putty. In Proceedings of the 12: International RILEM Workshop on Historic Mortars: Characteristics and Tests, Paisley, Scotland, 12–14 May 1999.
5. Rodriguez-Navarro, C.; Cazalla, O.; Elert, K.; Sebastian, E. Liesegang pattern development in carbonating traditional lime mortars. *Proc. R. Soc. Lond. A* **2002**, *458*, 2261–2273. [CrossRef]
6. Elert, K.; Rodriguez-Navarro, C.; Sebastian, E.; Hansen, E.; Cazalla, O. Lime Mortars for the Conservation of Historic Buildings. *Stud. Conserv.* **2002**, *47*, 62–75. [CrossRef]
7. Cazalla, O. Morteros de cal. Aplicación en el Patrimonio Histórico. Ph.D. Thesis, Universidad de Granada, Granada, Spain, 2002.
8. Rodriguez-Navarro, C.; Ruiz-Agudo, E.; Ortega-Huertas, M.; Hansen, E. Nanostructure and Irreversible Colloidal Behavior of $Ca(OH)_2$: Implications in Cultural Heritage Conservation. *Langmuir* **2005**, *21*, 10948–10957. [CrossRef] [PubMed]
9. Cultrone, G.; Sebastian, E.; Ortega Huertas, M. Forced and natural carbonation of lime-based mortars with and without additives: Mineralogical and textural changes. *Cem. Concr. Res.* **2005**, *35*, 2278–2289. [CrossRef]
10. Van Balen, K. Carbonation reaction of lime, kinetics at ambient temperatura. *Cem. Concr. Res.* **2005**, *35*, 647–657. [CrossRef]
11. Lawrence, R.M. A Study of Carbonation in Non-Hydraulic Lime Mortars. Ph.D. Thesis, University of Bath, Bath, UK, 2006.
12. Arandigoyen, M.; Álvarez, J.I. Proceso de carbonatación en pastas de cal con distinta relación agua-conglomerante. *Mater. Construcción* **2006**, *56*, 5–18.
13. Ruiz-Agudo, E.; Rodriguez-Navarro, C. Microstructure and rehology of lime putty. *Langmuir* **2009**, *26*, 3868–3877.
14. Mascolo, G.; Mascolo, M.C.; Vitale, A.; Marino, O. Microstructure evolution of lime putty upon aging. *J. Cryst. Growth* **2010**, *312*, 2363–2368. [CrossRef]
15. Gomez-Villalba, L.S.; López-Arce, P.; Alvarez de Buergo, M.; Fort, R. Atomic Defects and Their Relationship to Aragonite–Calcite Transformation in Portlandite Nanocrystal Carbonation. *Cryst. Growth Des.* **2012**, *12*, 4844–4852. [CrossRef]
16. Rosell Amigó, J.R. Aportaciones al Conocimiento del Comportamiento Deformacional de Pastas de cal: Tamaño y Formas de las Partículas y su Viscosidad. Ph.D. Thesis, Universitat Politècnica de Catalunya, Barcelona, Spain, 2013.
17. Guasch Ferré, N. Optimització de Mètodes Multitécnica per a la Caracterització de Components Orgànics i Morters de Calç tradicionals de l'antiguitat. Desenvulopament de Metodologies Experimentals per a la Seva Conservació i Restauració. Aplicació a un cas d'estudi: Els Estucs de la Pintura Mural de la Cultura Maia (Antiga Mesoamèrica). Ph.D. Thesis, Universitat Politècnica, de València, València, Spain, 2016.
18. Rodriguez-Navarro, C.; Burgos-Cara, A.; Di Lorenzo, F.; Ruiz-Agudo, E.; Elert, K. Nonclassical Crystallization of Calcium Hydroxide via Amorphous Precursors and the Role of Additives. *Cryst. Growth Des.* **2020**, *20*, 4418–4432. [CrossRef]
19. Michalopoulou, A.; Maravelaki, P.N.; Kilikoglou, V.; Karatasios, I. Morphological characterization of water-based nanolime dispersions. *J. Cult. Herit.* **2020**, *46*, 11–20. [CrossRef]
20. Kang, S.H.; Kwon, Y.H.; Moon, J. Controlling the hydration and carbonation in lime-based materials: Advantage of slow carbonation in CO_2 curable construction materials. *Constr. Build. Mater.* **2020**, *249*, 118749. [CrossRef]
21. Cizer, O.; Van Balen, K.; Elsen, J.; Van Gemert, D. Real-time investigation of reaction rate and mineral phase modifications of lime carbonation. *Constr. Build. Mater.* **2012**, *35*, 741–751.
22. Amigo, J.M.; Briansó, J.L.; Briansó, M.C.; Coy-Yll, R.; Soláns-Huguet, J. *Cristalografía*; Editorial Rueda: Madrid, Spain, 1981; p. 548.
23. Oriols, N.; Salvadó, N.; Pradell, T.; Butí, S. Amorphous calcium carbonate (ACC) in *fresco* mural paintings. *Microchem. J.* **2020**, *154*, 104567. [CrossRef]
24. Oriols, N.; Salvadó, N.; Pradell, T.; Jiménez, N.; Cotte, M.; Gonzalez, V.; Butí, S. Carbonation of fresco mural paintings with a dolomitic mortar. *Cem. Concr. Res.* **2022**, *157*, 106828. [CrossRef]

25. Pocostales, L. Procedimiento Para el Aislamiento y Estudio de la Capa Superficial de un Material Húmedo por Embutición. "Procedure for the Isolation and Study of the Surface Layer of a Wet Material through Encapsulation". N° de patente en la OEPMP20153165, 9 October 2015.

26. Dee, G.T. The patterns produced by precipitation at a moving reaction front. *Physica D* **1986**, *23*, 340–344. [CrossRef]

27. Dee, G.T. Patterns produced by precipitation at a moving reaction front. *Phys. Rev. Lett.* **1986**, *57*, 275–278. [CrossRef]

28. Viedma, C. Transferencia de Masa y Criterios Onto-Morfogenéticos en Sistemas Difusivos Finitos. Aplicación a la Síntesis de Yeso en gel de Sílice y Agar-Agar. Ph.D. Thesis, Universidad Complutense de Madrid, Madrid, Spain, 1989.

29. Pomar Gomà, L.; Ginés Gracia, A.; Ginés Gracia, J.; Moyà Niell, G.; Ramon Pérez de Rada, G. Nota previa sobre la petrología y mineralogía de la calcita flotante de algunas cavidades del levante mallorquín. *Endins Publicació D'espeleologia* **1975**, *2*, 3–6.

30. Gebauer, D.; Gunawidjaja, P.N.; Ko, J.Y.; Bacsik, Z.; Aziz, B.; Liu, L.; Hu, Y.; Bergstrom, L.; Tai, C.W.; Sham, T.K.; et al. Proto-Calcite and Proto-Vaterite in Amorphous Calcium Carbonates. *Angew. Chem. Int. Ed.* **2010**, *49*, 8889–8891. [CrossRef] [PubMed]

31. Wang, J.; Becker, U. Structure and carbonate orientation of vaterite ($CaCO_3$). *Am. Mineral.* **2009**, *94*, 380–386. [CrossRef]

32. Makreski, P.; Jovanovski, G. Minerals from Macedonia. IX. Distinction between some rhombohedral carbonates by FTIR spectroscopy. *Bull. Chem. Technol. Maced.* **2003**, *22*, 25–32.

33. Varas, M.J.; Alvarez de Buergo, M.; Fort, R. Natural cement as the precursor of Portland cement: Methodology for its identification. *Cem. Concr. Res.* **2005**, *35*, 2055–2065. [CrossRef]

34. Hughes, T.J.; Methven, C.M.; Jones, T.; Pelham, S.E.; Fletcher, P.; Hall, C. Determining Cement Composition by Fourier Transform Infrared Spectroscopy. *Adv. Cem. Based Mater.* **1995**, *2*, 91–104.

35. Vagenas, N.V.; Gatsouli, A.; Kontoyannis, C.G. Quantitative Analysis of Synthetic Calcium Carbonate Polymorphs Using FT-IR Spectroscopy. *Talanta* **2003**, *59*, 831–836. [CrossRef]

36. Andersen, F.A.; Brčević, L. Infrared Spectra of Amorphous and Crystallyne Calcium Carbonate. *Acta Chim. Scand.* **1991**, *45*, 1018–1024. [CrossRef]

37. Rodriguez-Blanco, J.D.; Shaw, S.; Benning, L.G. The kinetics and mechanisms of amorphous calcium carbonate (ACC) crystallization to calcite, via vaterite. *Nanoscale* **2011**, *3*, 265–271.

38. Coleyshaw, E.E.; Crump, G.; Griffith, W.P. Vibrational spectra of the hydrated carbonate minerals ikaite, monohydrocalcite, lansfordite and nesquehonite. *Biomol. Spectrosc.* **2003**, *59*, 2231–2239.

39. Poduska, K.M.; Regev, L.; Boaretto, E.; Addadi, L.; Weiner, S.; Kronik, L.; Curtarolo, S. Decoupling Local Disorder and Optical Effects in Infrared Spectra: Differentiating Between Calcites with Different Origins. *Adv. Mater.* **2011**, *23*, 550–554. [CrossRef] [PubMed]

40. Chu, V.; Regev, L.; Weiner, S.; Boaretto, E. Differentiating between anthropogenic calcite in plaster, ash and natural calcite using infrared spectroscopy: Implications in archaeology. *J. Archaeol. Sci.* **2008**, *35*, 905–911. [CrossRef]

41. Regev, L.; Poduska, K.M.; Addadi, L.; Weiner, S.; Boaretto, E. Distinguishing between calcites formed by different mechanisms using infrared spectrometry: Archaeological applications. *J. Archaeol. Sci.* **2010**, *37*, 3022–3029. [CrossRef]

42. Maciejewski, M.; Reller, A. Formation of Amorphous $CaCO_3$ during the Reaction of CO_2 with CaO. *Thermochim. Acta* **1989**, *142*, 175–188. [CrossRef]

43. Freeman, C.L.; Harding, J.H. The transformation of amorphous calcium carbonate to calcite and classical nucleation theory. *J. Cryst. Growth* **2023**, *603*, 126978. [CrossRef]

44. Gebauer, D.; Kellermeier, M.; Gale, J.D.; Bergstrom, L.; Colfen, H. Pre-nucleation clusters as solute precursors in crystallization. *Chem. Soc. Rev.* **2014**, *43*, 2348–2371.

45. Gebauer, D.; Cölfen, H. Prenucleation clusters and non-classical nucleation. *Nano Today* **2011**, *6*, 564–584. [CrossRef]